Chapter 6

Transmission Electron Microscopy for the Characterization of Cellulose Nanocrystals

Madhu Kaushik, Carole Fraschini, Grégory Chauve, Jean-Luc Putaux and Audrey Moores

Additional information is available at the end of the chapter

http://dx.doi.org/10.5772/60985

Abstract

Cellulose nanocrystals (CNCs) are high aspect ratio nanomaterials readily obtained from cellulose microfibrils via strong acid hydrolysis. They feature unique properties stemming from their surface chemistry, their crystallinity, and their three-dimensional structure. CNCs have been exploited in a number of applications such as optically active coatings, nanocomposite materials, or aerogels. CNC size and shape determination is an important challenge and transmission electron microscopy (TEM) is one of the most powerful tools to achieve this goal. Because of the specifics of TEM imaging, CNCs require special attention. They have a low density, are highly susceptible to electron beam damage, and easily aggregate. Specific techniques for both imaging and sampling have been developed over the past decades. In this review, we describe the CNCs, their properties, their applications, and the need for a precise characterization of their morphology and size distribution. We also describe in detail the techniques used to record quality images of CNCs. Finally, we survey the literature to provide readers with specific examples of TEM images of CNCs.

Keywords: cellulose nanocrystals, transmission electron microscopy, particle size, characterization, size distribution, sample preparation

1. Introduction

1.1. Native cellulose and the production of cellulose nanocrystals

Cellulose, the most abundant biopolymer on Earth, has been extensively used by man, in the form of macro- and microstructures, as a traditional resource in many aspects of daily life, notably to produce textiles and papers. This polymeric material is biosynthesized by a wide variety of living species such as plants, animals, bacteria, and some amoebas. Glucose is polymerized by enzymes in a continuous fashion. The resulting cellulose chains are homopolymers of β-1,4-linked anhydro-D-glucose units which associate to form microfibrils, further assembled into macrofibers and fibers. Crystalline and disordered regions alternate along the microfibrils (Figure 1a) [1-4].

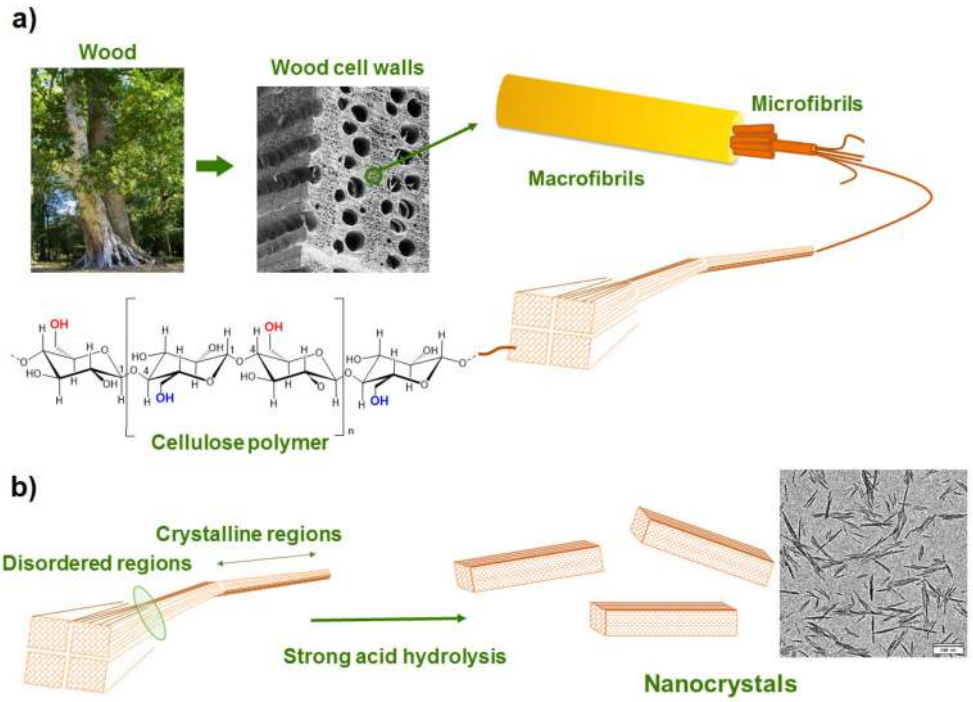

Figure 1. (a) Structural hierarchy of the cellulose fiber components from the tree to the anhydroglucose molecule (SEM image of wood cell structure: courtesy of D. Dupeyre, CERMAV); b) preparation of nanocrystals by selective acid hydrolysis of the disorganized regions of cellulose microfibrils (TEM image of cotton CNCs: courtesy of CERMAV).

In the late 1940s, cellulose crystallites were isolated for the first time by chemical treatment of a cotton substrate in hot concentrated sulfuric acid [5]. Soon after, Rånby showed that stable colloidal suspensions of negatively charged cellulose particles could be obtained [6, 7]. During

http://dx.doi.org/10.5772/60985

the extraction process, the cellulosic fibrous structure is broken down in the presence of concentrated sulfuric acid (other mineral acids can be used such as HCl). After diffusion of the acid within the substrate, the glycosidic linkages in disordered regions, more accessible and reactive, are preferentially broken. An additional mechanical or ultrasound treatment results in the release of rodlike cellulose crystallites, so-called cellulose nanocrystals or CNCs (Figure 1b). Consequently, as the hydrolysis proceeds, the degree of polymerization of the cellulose macrostructures decreases, while the crystallinity of the nonsoluble particles increases [8].

1.2. Cellulose nanocrystal properties

In the early 1950s, detailed characterizations of the shape and size of various CNCs (cotton, ramie [9], and bacterial cellulose [10]) were proposed from transmission electron microscopy (TEM) images. Since then, CNCs have been produced from a wide (and expanding) variety of sources [11] such as wood (Figure 2a), cotton (Figure 2b), bamboo (Figure 2c) [12], bacteria (Figure 2d) [13], algae (Figure 2e), tunicates (Figure 2f) [14], eucalyptus [12], spruce bark [15], corncob [16], etc. The CNCs are rodlike objects with a length typically ranging from 50 to 1000 nm and a width varying from 3 to 50 nm (Table 1). CNCs thus have high length-to-width (aspect) ratios (10-100) [17-22]. Their morphology depends on the cellulose source and the conditions of preparation (type and concentration of acid, acid-to-cellulose ratio, reaction time, and temperature) (Figure 2). The nanoscopic features of the resulting CNCs considerably influence their colloidal and macroscopic properties such as suspension rheology, phase separation concentration, liquid crystal behavior, orientation under electric or magnetic field, and mechanical reinforcement ability in nanocomposites [14, 16].

CNCs can be prepared in different forms. First, CNCs can be manipulated in the form of acidic aqueous suspensions resulting from the strong acid hydrolysis of microfibrils or as neutral suspensions after neutralization. Subsequent surface modifications can be achieved *via* chemical treatment [23, 24]. Alternatively, different drying methods may be used to afford a fluffy material, with the aspect of white sugar candy [25].

In 1959, Marchessault *et al.* revealed that the chemical reaction of sulfuric acid with hydroxyl groups at the surface of cellulose CNCs formed sulfate ester groups, resulting in electrostatic repulsions between the particles and ensuring colloidal stability. Moreover, the authors showed that CNCs could self-organize into liquid crystalline phases [26].

The sulfuric acid hydrolysis of cellulose has remained confined to academic research laboratories until a big step was made in the mid 1990s, when it was shown that CNCs were efficient reinforcing fillers in latex-based polymer matrices, opening a new potential market for this high-end material [14, 27]. Since then, CNCs have become intensively studied with an accelerating rate of publications released each year [17-22]. Beside mechanical properties, colloidal properties of CNCs in suspension generated a series of studies investigating their ability to form liquid-crystal phases. The colloidal suspensions of CNCs spontaneously organize into a chiral nematic phase above a certain critical concentration. As a consequence, CNCs have been used to produce iridescent and birefringent films [28-31], chiral mesoporous silica [32, 33] and carbon [34], gold nanoparticle films with chiral plasmonic properties [35], enantioselective amino acid hydrolysis catalysts [36], hydrogels [37], and aerogels [38].

Moreover, the high surface area and controllable surface chemistry of CNCs make them a unique support for metal nanoparticles (NPs) [39] CNC supported NPs, including Pd [40] and Au [41], were used as nanocatalysts. Pd NPs distributed onto CNCs were used for hydrogenation and carbon-carbon bond coupling reactions [40, 42-44], while the Au counterparts were used for 4-nitrophenol reduction [45]. Ag NPs were also deposited onto CNCs and the resulting material featured antibacterial activity [46].

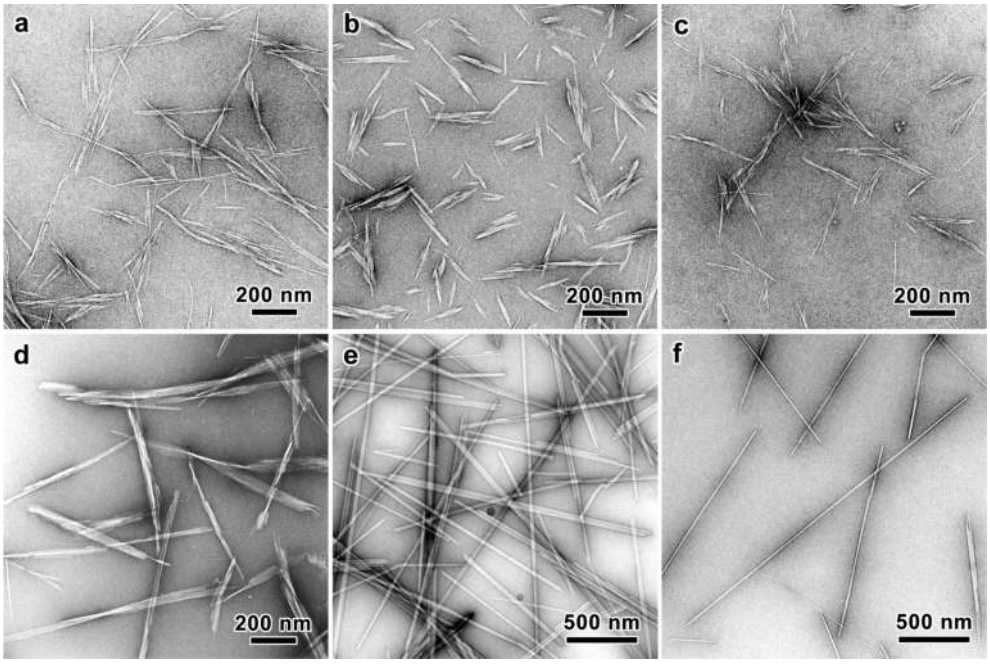

Figure 2. TEM images of negatively stained preparations of CNCs of various origins: a) wood (courtesy of G. Chauve, FPInnovations); b) cotton (courtesy of F. Azzam, CERMAV); c) bamboo (courtesy B. Jean, CERMAV; d) *Gluconacetobacter xylinus* (courtesy of H. Bizot, INRA); e) *Glaucocystis* (courtesy of Y. Nishiyama, CERMAV); f) *Halocynthia papillosa* (courtesy of A. Osorio-Madrazo, A. Ludwig University of Freiburg).

This large panel of high-end applications strongly encouraged industry to achieve large-scale production of CNCs. The forest-based industry in North America, Northern Europe, and Japan is currently looking into renewing and reinventing itself to extend its activities and guarantee its survival, while renewable materials are being increasingly appealing as fossil-based material replacement. In addition, CNCs are inherently safe, practically nontoxic materials [47]. Nanocellulose-based, value-added materials definitely constitute promising vectors to "turn wood into gold" and revive the forest-based industry. These combined factors led to the opening of the first commercial plant by CelluForce Inc. (Windsor, Québec, Canada), producing 1 ton of CNCs per day [48].

http://dx.doi.org/10.5772/60985

Several review articles and books have been published over the last few years which cover in detail the various aspects of the CNC features and applications [17, 18, 20, 21, 49].

1.3. Need for CNC characterization

CNCs possess appealing properties in direct relation with their three-dimensional (3D) structure, including well-defined shape, size, and aspect ratio. From an industrial perspective, it is essential to collect reliable data on CNCs, especially for quality control, toxicology assessment, R&D and applications.

1.3.1. Quality control

The large-scale production of CNCs became a reality when CelluForce Inc. started up its demonstration plant. Getting reliable, fast, and accurate measurement of the particle size is a key to guarantee a consistent production of high-quality CNCs. Several methods exist (*vide infra*) to determine the size, size distribution, and shape of CNCs. So far, they are typically used in academic studies and provide a fairly consistent understanding of the material structure. However, for the moment, no systematic and streamlined method exists for size determination and evaluation of polydispersity for anisometric nano-objects such as CNCs. This question is particularly acute for large-scale quality control, for instance, in pilot plant production and beyond.

1.3.2. Toxicology assessment

Manufactured nanomaterials have recently caused societal concerns about their possible adverse effects on health and safety. Properties of nanomaterials typically differ from those of their parent bulk materials because of their larger surface area, leading to a greater activity, their smaller size, resulting in their ability to cross natural barriers, and intrinsic effects caused by nanometric size, including electronic and plasmonic effects. Since such particles may have a negative effect on biological systems and ecosystems, their toxicological risks must be evaluated and an accurate description of the product in terms of dimensions, chemistry, and toxicity is required by the authorities. CNCs have extensively been evaluated using standard ecotoxicological and mammalian test protocols and have, to date, been shown to be practically nontoxic in each of the individual tests [47]. In addition, CNCs have recently obtained regulatory approval under Canada's New Substances Notification Regulations (NSNR) for unrestricted use in Canada and is the first organic nanomaterial to be added to Canada's domestic substance list.

1.3.3. R&D and applications

To maximize the reinforcing or liquid crystal behavior potential of CNCs, the particles have to be as well-dispersed as possible, especially in nanocomposite applications. An aspect that can lead to aggregation/agglomeration and then affect the further redispersion of the particles is mainly the final drying stage. Drying is a critical process for the large-scale industrial production of CNCs. Aqueous suspension leads to bacterial contamination and precludes

long-term storage. In addition, the cost associated to the transportation of suspensions containing up to 90% water is not economically viable. Various drying processes can be used such as freeze-drying, supercritical drying, spray-drying, oven drying, and air drying. Spray-drying methods are used in the industrial production of CNCs. The resulting solid, hornified macrostructure may be difficult to further redisperse, even in water. Neutralization of the acidic sulfate ester groups prior to drying helps with redispersion [25].

1.3.4. Challenges regarding CNC particle size measurement

The aspect ratio of CNCs dictates the percolation threshold, a key parameter to control mechanical properties in nanocomposites. Knowing the size and morphology of CNCs with precision plays a key role in the development of numerous applications where these features directly impact the properties of the final product. CNCs prepared by sulfuric acid hydrolysis of cellulose substrates are rigid, acicular-shaped and highly crystalline nanoparticles. The geometrical dimensions of these rodlike crystallites vary exceedingly with the source of cellulose (Table 1) and with the hydrolysis reaction conditions. For example, CNCs extracted from wood are 3-7 nm in width and 100-200 nm in length, while CNCs derived from tunicate are 10-20 nm in width and 500-2000 nm in length [14]. These values are indicative as different reaction conditions result in different sizes and size distributions. Indeed, size distributions were published as early as 1944 for ramie and cotton CNCs [50]. Lists of the different sizes of CNCs extracted from various sources can be found in recent reviews [17, 18, 20, 21] and in Table 1. The size distribution may have an impact on the properties and thus the applications of CNCs. For instance, it has been shown that polydispersity influenced the phase separation behavior of liquid crystalline suspensions [51, 52]. CNCs are usually obtained as colloidal aqueous suspensions and the production process induces batch-to-batch particle size variability. The rheological properties of the suspension and the state of individualization of the particles are strongly affected by external parameters such as nanoparticle concentration, pH, ionic strength, temperature, or the presence of an additional compound or impurities [53-55]. The stability of the suspension is due to the electrostatic repulsion forces created by the negatively charged sulfate ester groups located at the surface of the crystals. More generally, their propensity to agglomerate is driven by their surface chemistry. For example, the addition of electrolyte screens the surface charges of the particles, reducing the electrostatic repulsion that prevents CNCs from agglomerating, which results in either an increase or a decrease of the measured particle size by photon correlation spectroscopy (PCS) depending on the amount of electrolyte introduced. Since CNC particles do not undergo swelling or compaction upon the addition of electrolyte, this increase/decrease of the measured particle size is a pure artifact driven only by the laws of physics and thermodynamics. Consequently, for a given sample, particle size variability depends on the sample preparation conditions and the measurement techniques.

Particle size is a good indicator of the quality of the CNC dispersion but the direct observation of nanoparticles remains a challenge and high-resolution direct imaging or light scattering techniques are required.

http://dx.doi.org/10.5772/60985

1.4. Microscopy and spectroscopy techniques used for CNC characterization

As previously mentioned, CNCs come in a wide variety of length, width, and shape depending on the cellulose sources. The cross sections of CNCs also display a variety of shapes, e.g., square, rectangular, or parallelogram, that are dictated by the arrangements of enzymatic terminal complexes extruding cellulose chains during the biosynthesis. As shown in different cases, the edges of the crystals can be eroded during the acid hydrolysis yielding hexagonal or octagonal cross sections exposing small surface area of hydrophobic (200) planes [56].

Many instruments are commonly used for the determination of particle size distribution (PSD) and particle dimension(s), each instrument detecting size through its own physical principle. Numerous techniques based on microscopy, light interactions, electrical properties, sedimentation, sorting, and classification allow access to particle size. Depending on the technique, the results are more or less accurate and are related to the nanoparticle shape and its physico-chemical features such as chemical composition, heterogeneity, topography, surface charge density, dispersing medium, viscosity, etc. The morphology of CNCs can be accurately revealed either by microscopic methods including transmission electron microscopy (TEM), cryo-TEM, atomic force microscopy (AFM), field emission gun scanning electron microscopy (FEG-SEM), or by scattering techniques such as polarized and depolarized light scattering (DLS and DDLS, respectively) and small- and wide-angle neutron or X-ray scattering (SANS, WANS, SAXS, and WAXS, respectively). Each of these techniques has its own advantages and limitations in their application to the study of CNCs. Consequently, care should be taken while comparing particle size data obtained from different techniques.

Light scattering techniques rely on the interaction of light with the hydrodynamic volume of a particle. With anisometric nanoparticles, the response varies as a function of the orientation of each individual particle. The collected data thus need to be mathematically processed to extract meaningful information. Typically, for acicular particles, such as CNCs, light scattering techniques have not been able to match the precision of microscopy. Microscopy, on the other hand, provides direct images of individual particles and allows characterization of its morphology and size (length, width and thickness). Microscopy techniques which have the nanometer scale resolution capabilities to image CNCs are electron microscopy and AFM. Electron microscopy enables the direct observation of the dimensions (*i.e.,* length and width) of a given particle. AFM provides information on morphology, surface topography, mechanical properties, and adhesion of CNCs under ambient conditions [15, 16, 57, 58]. While AFM provides reliable information on the thickness of the particles deposited on a flat substrate, the lateral resolution is limited by the convolution of the tip end, whose size and curvature are significantly larger than the dimensions of the nano-objects. However, this so-called tip-broadening effect can sometimes be deconvoluted [59]. On the contrary, TEM images provide good nanometric (and often subnanometric) lateral resolution, allowing to rapidly screen a large population of particles, thus avoiding major sampling issues. However, as TEM images are projections of the objects along the incident beam direction, it may be difficult to accurately measure the particle thickness. Moreover, the low density of CNCs calls for the use of staining methods. These limitations may be overcome by some of the recent developments described in the following sections, including low-dose microscopy and 3D imaging. When possible, the

combination of data from AFM and TEM images, and scattering analyses provides an optimal description of the particle morphology. For instance, a combination of imaging and scattering data was used by Elazzouzi-Hafraoui *et al.* [60] and Brito *et al.* [12] to precisely describe the morphology of CNCs extracted from a variety of sources.

It has to be noted that due to significant technical progress in instrumentation (low-voltage and beam-decelerated imaging, variable pressure) and detector variety and sensitivity, FEG-SEM imaging has become a perfectly valid approach to visualize the surface of CNC assemblies from dried systems [61] or fractured chiral nematic films [62]. CNC suspensions dried on TEM grids can be observed as well in an SEM equipped with a detector located below the specimen. With this so-called scanning transmission electron microscopy (STEM) mode, transmitted and scattered electrons can be collected to reconstitute an image of the specimen very similar to those obtained with a TEM. Although the accelerating voltage is lower (10-30 kV) than that used in a TEM (100-300 kV), the resolution is sufficient to see the fine details of CNCs [11].

This chapter focuses on TEM approaches. We describe several methods to prepare CNC specimens and emphasize the specific conditions to observe these highly beam-sensitive nanoparticles in order to provide images of CNC dispersions and determine reliable size distributions. A thorough description of sample preparation procedures and observation techniques is followed by a review of the literature on CNC imaging by TEM.

2. TEM techniques used for the observation of CNCs

2.1. Selected milestones in the characterization of nanocellulose by TEM

TEM imaging and electron diffraction played a significant role in the morphological and structural studies of cellulose microfibrils and nanocrystals, complementing data from spectroscopic (Fourier-transform infrared spectroscopy and solid-state NMR) and scattering (of X-rays or neutrons) analyses. Important information was obtained at a local scale, allowing to identify mechanisms at work during the biosynthesis and biodegradation of cellulose crystals and characterize some physical properties, with or without additional chemical modification, inside cell walls or, after extraction, in suspension or incorporated in nanocomposite materials.

In 1940, H. Ruska (brother of E. Ruska, inventor of the TEM) published what can be considered to be the first images of microfibrils obtained after HCl hydrolysis of cotton cellulose [63]. During the following two decades, the progress in TEM imaging of cellulose was mostly driven by the motivation to characterize the submicrometer structure of natural cellulose fibers. However, the identification of smaller constituting elements required the disintegration of cell walls and fibers using strong mechanical and/or chemical treatment [26, 64-68]. In particular, images of individual crystalline "fragments" (not yet called CNCs) were recorded after strong sulfuric acid hydrolysis of celluloses from various sources [9, 10, 69, 70].

In parallel to these morphological studies, important structural information was obtained using electron diffraction. Fiber diffraction patterns were collected from *Valonia* cell wall

http://dx.doi.org/10.5772/60985

fragments and microfibrils, at room [71] and low [72] temperature, confirming at a local scale the longitudinal orientation of the cellulose chains. The size and distribution of crystallites were determined in *Valonia* microfibrils using diffraction contrast imaging [73]. Later on, electron diffraction was notably used to validate the existence of separate regions of Iα and Iβ allomorphs of cellulose in microcrystals from *Microdictyon* cell wall fragments [74]. TEM imaging and diffraction methods were also combined to demonstrate that the biosynthesis of bacterial cellulose ribbons occurred by addition of the cellulose precursors at the nonreducing end of the chains [75]. A further striking demonstration of the molecular order in cellulose crystallites was provided when Sugiyama *et al.* successfully recorded the first high-resolution images directly showing longitudinal and axial projections of the crystal lattice of *Valonia* microfibrils [76, 77].

2.2. Sample preparation

The sample for TEM imaging has to be extremely thin in order to be transparent to electrons. Sample preparation is thus a crucial step. The limiting thickness depends on the atomic number and density of the observed material and on the energy of the incident electrons. Typically, for polymers, the thickness should remain well below 1 μm. For bulk materials, preparing such a thin specimen requires specific sectioning procedures. However, as the thickness of individual CNCs is well below this limit, the preparation of TEM specimens, for instance from dilute suspensions, is a lot easier.

2.2.1. Grids, supporting films and homogeneous distributions of nano-objects

In order to be observed by TEM, nanoparticle suspensions are deposited on 3.05-mm-large thin circular metallic grids with typical meshes around a few tens of micrometers, which will be placed in the sample holder for microscopy. There is a huge variety of TEM grids available and the selection of the right kind of grid is a crucial step for acquiring good images. Copper grids are the cheapest and the most widely used. However, when the pH of the suspension is low or high, copper can be degraded, resulting in the formation of artefactual crystallites or dendrites upon drying. In that case, gold or nickel grids have to be preferred. Carbon is by far the most commonly used supporting film. Carbon-coated grids are available commercially but carbon films can also be prepared in the laboratory by evaporating carbon on sacrificial collodion films or cleaved mica. The resulting films are then "fished" on copper grids. Carbon films have a typical thickness of 5-20 nm, depending on whether transparency or mechanical stability is favored. Formvar is also used as supporting film but it is less electron-transparent than carbon and can drift when heated by the electron beam at high magnification.

The main challenge in preparing a specimen suitable for TEM observation is to ensure a satisfying dispersion on the various objects. This is particularly critical when one wants to determine the size distribution of a population of CNCs. The supporting carbon film is initially rather hydrophobic, so the deposition of aqueous suspensions and subsequent air-drying generally result in locally accumulated material. Glow discharge is considered to be the easiest and most efficient pretreatment of carbon films before sample deposition. The TEM grids then are placed in the chamber of a glow discharge unit (*e.g.*, automated commercial systems like

easiGlow from Pelco or ELMO from Agar Scientific). A pumping system allows to reach a low pressure and the residual air is ionized. The grids are submitted to this mild plasma cleaning during a few seconds, which results in a hydrophilic carbon surface (at least during several minutes) onto which aqueous suspensions easily spread. As charges are also generated on carbon during the treatment, the nano-objects tend to adsorb on the surface. The excess of liquid can thus be gently blotted out without waiting for complete drying and the objects should be homogenously distributed on the grid. An example of a distribution of cotton CNCs prepared after glow discharge of the carbon film is shown in Figure 3a. The factory settings of the commercial systems generally promote negative charges and hydrophilic surfaces but, depending on the applications and systems, positive charges and/or hydrophobic surfaces can be produced using additional agents.

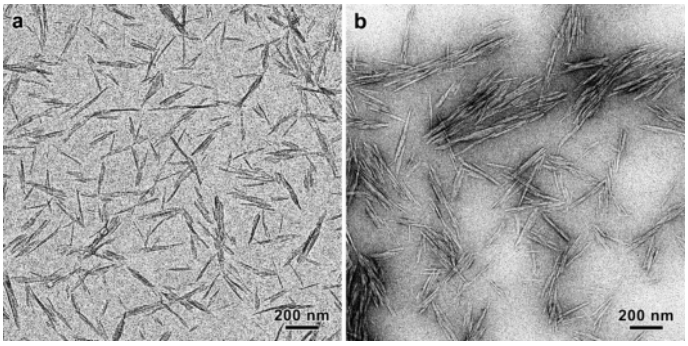

Figure 3. Comparison of images of unstained (a) and negatively stained (b) preparations of cotton CNCs. In both cases, the suspensions have been deposited on freshly glow-discharged carbon-coated grids.

Different materials have been tested as supporting films. While hydrophobic formvar promoted aggregation (Figure 4a), satisfactory dispersions of individual CNCs were achieved on hydrophilic silicon monoxide (Figure 4b) [78]. Silica (SiO_2) and silicon nitride (Si_3N_4) films, with or without additional functionalization, are also commercially available (NanoGrids from Dune Sciences).

In addition to the choice of supporting film and the use of an additional pretreatment, the use of very dilute suspensions is recommended, typically 0.001-0.01 % (w/v) for CNC suspensions. The nanocrystals will adsorb more efficiently onto hydrophilic films and particularly those that have been glow-discharged and this effect can be compensated by a higher dilution.

2.2.2. Impact of the CNC suspension on the TEM observation

After acid hydrolysis, CNCs occur in the form of suspensions that generally require further purification steps to remove the residual acid and salts. Indeed, residual soluble salts will likely crystallize upon drying on the supporting film of the TEM grid, resulting in the formation of artifactual dendrites. The suspensions are dialyzed against water to reach a pH around 2.5-3. Then CNCs may be used as such – *i.e.*, in the form of an acidic aqueous suspension – or may

http://dx.doi.org/10.5772/60985

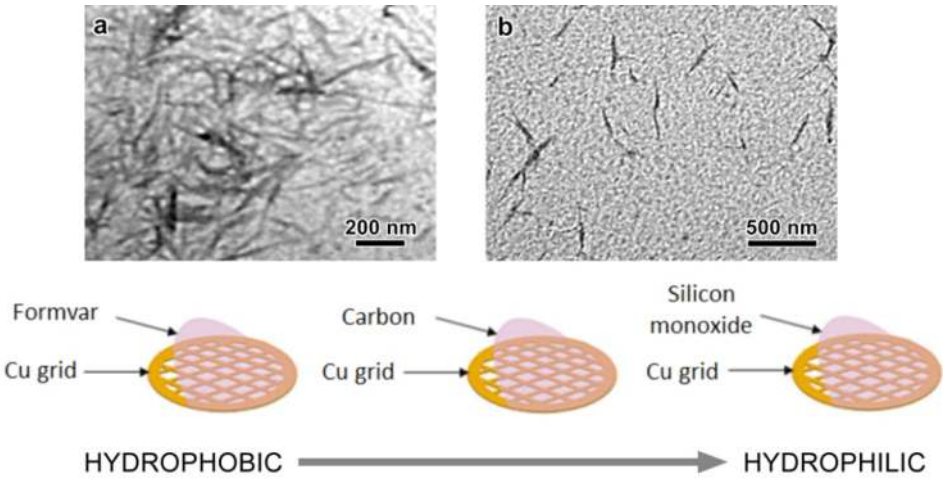

Figure 4. Comparison of never-dried CNCs at pH 5-6 on different types of supporting films: a) formvar; b) silicon monoxide (reproduced from [78] by permission of the KTH Royal Institute of Technology).

be neutralized with NaOH to reach pH~7, and be used in the form of neutral aqueous suspension [25]. The drying step of an acidic CNC suspension prevents the CNCs to be later redispersed in water because CNC aggregates are created by hydrogen bonds *via* a phenomenon called hornification. Adjusting the suspension to a neutral pH prior to drying allows the dried CNCs to be spontaneously redispersed in water, while the specimens dried from acid pH suspensions cannot be properly resuspended [25].

The impact of the drying step of the CNCs prior to resuspension has been demonstrated by comparing three TEM specimens: 1) "never-dried" CNCs – CNC suspensions resulting directly from cellulose hydrolysis, 2) "freeze-dried" CNCs – CNC suspensions made from dispersing pH-neutralized freeze-dried CNCs, and 3) "spay-dried" CNCs – CNCs suspension made from dispersing pH-neutralized spray-dried CNCs [78]. For all three specimens, the pH of the redispersed suspension was adjusted to 5-6 and the suspensions were deposited on carbon-coated grids. As seen in Figure 5, dispersions from spray-dried samples featured more CNC aggregates than those prepared from freeze-dried and never-dried samples. More single rods were observed in the latter than in any of the other two. On Figure 5a, the typical width of the observed bundles in the three samples is marked and is indicative of the degree of aggregation. This conclusion is actually consistent with the fact that spray-dried CNCs are more difficult to disperse than freeze-dried or never-dried counterparts [25]. In addition, a mushroom-like morphology has been exclusively reported for the spray-dried CNCs, which look like patches, with a size ranging from 100 to 200 nm, with a much higher contrast than the rods [79, 80]. However, this morphology was proved to be an artifact from improper dispersion of the sample on the TEM grid [78]. Additionally, the suspensions of previously dried CNCs could be briefly sonicated to promote greater dispersion before preparing TEM grids.

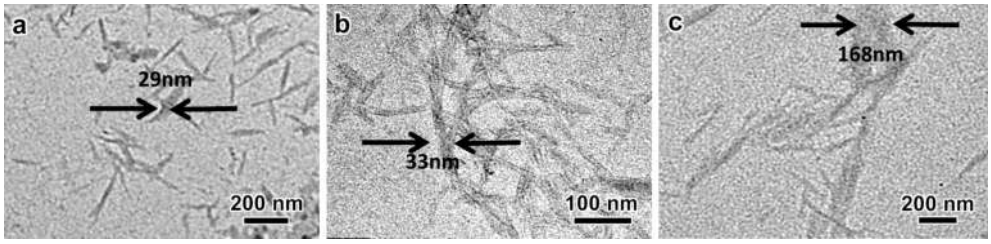

Figure 5. TEM images of unstained wood pulp CNCs: a) from a suspension of never-dried CNCs; b) from a freeze-dried suspension of redispersed CNCs; c) from a spray-dried suspension. All suspensions were adjusted to pH 5-6 before deposition onto carbon-coated copper grids (reproduced from [78] by permission of the KTH Royal Institute of Technology).

The pH of CNC suspensions before TEM sample preparation has a clear influence on the CNC dispersion on the grid. When CNCs are redispersed in dionized water, the pH is around 5-6. If never-dried CNCs are observed at this pH, on carbon-coated TEM grids, the images show both individual and aggregated CNCs (Figure 6). Theimproved CNC dispersion on the grid is obtained at pH 3.5. Indeed, at pH below 4-5, CNCs are more negatively charged as the half-sulfate ester groups are in their acidic form.

The particle morphology and aggregation state observed by TEM depends on how the dried CNC sample has been redispersed in water (use of sonication to promote de-agglomeration), which in turn depends upon the drying history of the CNCs (*i.e.*, the pH of the suspension before drying). The optimal conditions to image CNCs is to prepare a TEM specimen from a suspension of never-dried CNCs or a pH-neutralized suspension.

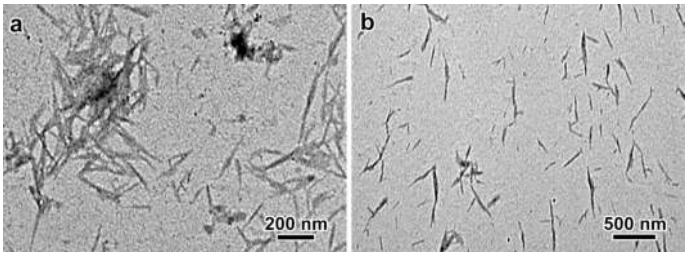

Figure 6. Influence of the pH of the CNC suspension on the dispersion on carbon films: a) pH 5-6; b) pH 3.5 (reproduced from [78] by permission of the KTH Royal Institute of Technology).

2.2.3. Contrast enhancement techniques

2.2.3.1. Negative staining

Since the contrast of cellulose specimens is rather low, and since using high magnification to see more details will result in a rapid degradation of the particles (hence a loss of contrast),

http://dx.doi.org/10.5772/60985

several techniques may be used to enhance the contrast in the images. The most widely used is commonly called negative staining. A drop of an aqueous solution of heavy atom salts is deposited on the specimen. Upon drying, a thin layer of heavy atoms concentrate around the nanoparticles, creating an electron dense outline [81]. The CNCs thus appear as clear objects on a dark background, hence the negative effect on the image. The preparations can be observed at a higher magnification as, although cellulose is indeed damaged by the electron beam, the heavy atom "imprint" is resistant, revealing fine details of the surface topography. So far, 2% (w/v) uranyl acetate solutions have been the most commonly used stain but phototungstic acid or ammonium molybdate are sometimes used as well. Uranyl acetate will likely disappear from the catalogues as recent regulations have been enforced regarding the handling of radioactive products, resulting in a significant price increase. Consequently, new commercial ready-to-use stain solutions have been recently proposed, such as Uranyless (that contains lanthanides, from Delta Microscopies) or NanoVan (methylamine vanadate, from Nanoprobes). Practically, a homogenous negative staining of CNCs will be achieved under two conditions: i) the supporting carbon film has to be glow-discharged before the nanoparticles and the stain are deposited; ii) the negative stain has to be deposited on the specimen before drying. After a few minutes, the stain in excess can be blotted away with filter paper and the residual thin stain film allowed to dry. It has to be noted that negative staining can partly promote the local flocculation of the CNCs on the supporting film, as can be seen in Figure 3b.

2.2.3.2. Metal shadowing

The technique has been used very early on to observe nanocellulose. Indeed, in the 1950s, Rånby published images of metal-shadowed preparations of wood and cotton microfibrils [10], as well as tunicate [70] and bacterial CNCs [10]. Images of ramie and cotton CNCs can also be found in Mukherjee and Woods' paper [9]. Metal (generally gold/palladium or platinum) is vaporized on the sample with a given incidence angle. It thus accumulates on one side of the nanoparticles (electron-dense region) and is absent on the other side (electron-transparent region). This results in a shadow-and-light effect that enhances the topography details of the specimen with a very high contrast. Again, it is the metallic layer that is observed even if the cellulose particles are damaged by the incident electron beam. The resolution is limited by the granularity and thickness of the metal film that increases the apparent width of the particles.

In the specific case of concentrated CNC suspensions, freeze-fracture can be used. A drop of the suspension is fast frozen and, under vacuum, a sharp knife breaks the frozen specimen into two fragments. The resulting surfaces are then directionally shadowed with a thin layer of evaporated metal, consolidated with an additional layer of carbon. The specimen is then warmed up and the metallic replica washed, deposited on a carbon-coated grid, and observed in the TEM, providing a high-contrast image of the topography of the fractured surface. An example of freeze-fracture replica of a concentrated suspension of cotton CNCs is shown in Figure 7a.

2.2.4. Cryo-TEM

Cryo-TEM consists in observing nanoparticles embedded in a thin film of transparent vitreous ice, thus avoiding the detrimental effects of drying and/or staining (degradation, deformation, aggregation, agglomeration, coalescence, uniplanar orientation, buffer salt crystallization, etc.). This technique is particularly helpful with dilute suspensions of nano-objects that are soft or liquid at room temperature and whose morphology or structure may be affected by air-drying (deformation due to capillary forces, decrystallization). Droplets of suspensions are typically deposited on holey or lacey (*e.g.*, NetMesh from Pelco) carbon films supported by TEM copper grids. Perforated support foils with predefined hole size and arrangements (*e.g.*, Quantifoil from Quantifoil Micro Tools or C-flat from Protochips) can also be used. The liquid in excess is blotted with filter paper and the thin remaining film is quench-frozen in liquid ethane [81]. The frozen specimen is mounted in a cryo-specimen holder precooled with liquid nitrogen, transferred in the microscope, and maintained at low temperature during TEM observation. Temperature- and humidity-controlled chambers with automated plungers are commercially available (Vitrobot from FEI, EM-GP from Leica or Cryoplunge from Gatan), ensuring a higher reproducibility of the fast-freezing procedure. Cryo-TEM is not limited to aqueous suspensions and organic solvents can also be used, provided that they can be properly vitrified and that they are not dissolved in liquid ethane.

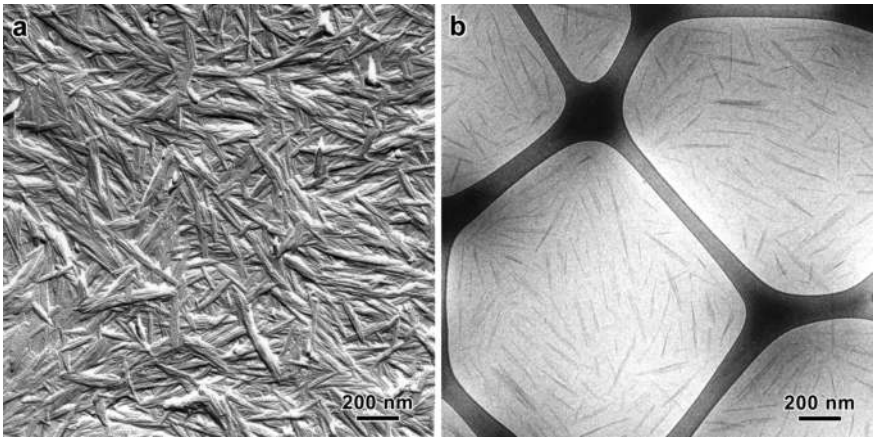

Figure 7. Alternative methods to observe cotton CNC dispersions: a) Pt/C replica of a freeze-fractured concentrated suspension; b) cryo-TEM preparation of a dilute suspension. The CNCs are embedded in a thin film of vitreous ice (courtesy of S. Elazzouzi-Hafraoui, CERMAV).

In the case of CNCs which are rigid crystalline nanoparticles, using cryo-TEM is helpful to prevent the aggregation that may happen upon drying, resulting in unwanted particle superimposition. Indeed, cryo-TEM has only been used in a small number of cases, to observe unstained nonflocculating cotton CNCs (Figure 7b) [60, 82] and characterize by electron tomography (see § 2.3.3) the 3D shape of CNCs wrapped with dendronized-polymers [62] or covered with Pd patches [44].

2.2.5. Ultramicrotomy

This preparation technique should be used for bulk materials like plant tissues, cell wall fragments, nanocomposite materials, fibers, etc. When the specimen is affected by air-drying, it has to be first fixed in paraformaldehyde/glutaraldehyde, post-fixed with osmium tetroxide, dehydrated by exchange with ethanol and embedded in hardening resins (Epon, LR White, Spurr, etc.) [83]. In the case of nanocomposite materials incorporating cellulose microfibrils (CMFs) or CNCs as reinforcing fillers, small fragments can be used without resin-embedding, provided that the material is sufficiently hard. Ultrathin (50-150 nm) sections of the specimens are then cut at room temperature with a diamond knife in an ultramicrotome [84]. The sections are collected on bare or carbon-coated TEM grids and, if necessary, in order to enhance contrast, may be post-stained with uranyl acetate/lead citrate. When the sample is soft at room temperature, ultrasectioning has to be performed in cryogenic conditions with a dedicated unit.

2.3. Observation techniques

Beside the constraints directly related to sample preparation (drying, staining, etc.), the TEM observation of CMFs and CNCs should result in the recording of images with a good signal-to-noise ratio and showing enough fine details of the objects. The various contrasts observed in the images are generated by physical interactions of the incident electrons with the material [85] and these contrasts have to be properly recorded by a sensitive "detector." Although for many years, micrographs were recorded on films, those have been progressively replaced by digital cameras typically equipped with a 1k×1k, 2k×2k or 4k×4k pixel-large CCD or CMOS detector. These cameras have wide dynamics, good linearity, and are very sensitive, allowing to record images with short exposure times and low electron doses. In addition, the software that pilots the camera can process the signal in real time, allowing, for instance, to calculate Fourier transform and correct some aberrations.

2.3.1. Contrast

Three main phenomena contribute to the overall contrast of CNCs in an image. Mass/thickness contrast (also called amplitude or diffusion contrast) is generally low for polymer particles as they are mostly composed of light elements that weakly scatter electrons. The proportion of electrons transmitted and scattered by the specimen depends on its density and thickness. By inserting an aperture located in the back focal plane of the objective lens, the operator blocks a certain amount of scattered electrons and form an image with the transmitted (or weakly scattered) electrons. In this so-called bright field image, the dark regions thus correspond to the ones scattering electrons the most. As CMFs and CNCs are generally very thin, they generate a low amplitude contrast which, as described in § 2.2.3, can be significantly enhanced by using specific staining techniques involving heavy atoms. However, for unstained preparations, large differences in contrast can be observed in hybrid organic-inorganic systems, allowing, for instance, to locate metallic or oxide nanoclusters distributed along cellulose nanoparticles [40].

Diffraction contrast occurs when the specimen is crystalline or semicrystalline, independently of its chemical nature (light or heavy atoms). Depending on the orientation of the crystal with respect to the incident beam, the electrons will be diffracted away from the optical axis. The set of discrete diffraction angles is defined by the unit cell of the crystal and can be determined using Bragg's relation [85]. When a diffracted beam is stopped by the objective lens aperture, in images with negative defocus, the regions of the particle from which the diffracted beam originates are very dark against the clear amorphous carbon background. This effect is thus important to visualize CNCs in bright field mode as it compensates somewhat the low amplitude contrast. It depends on the crystallinity index of cellulose (low for wood and high for tunicate CNCs, for instance). However, as cellulose is highly sensitive to beam damage, the diffraction contrast lasts for a limited time and disappears as soon as the material becomes amorphous.

Phase contrast is crucial in the case of electron-transparent nano-objects. It results from sharp differences in scattering properties between regions of the specimen. This is the case for CNCs spread on a carbon film (particles in vacuum), and CNC suspensions observed by cryo-TEM (particles embedded in vitreous ice). Phase contrast generates interference Fresnel fringes whose amplitude and distribution depend on the defocus of the objective lens [85]. The effect of phase contrast on the image of unstained CNCs is illustrated in Figure 8a and 8c. High defocus values (positive or negative) increase contrast but also generate larger Fresnel fringes and increase the apparent size of the nanoparticles. Note the complete reverse of contrast between underfocused and overfocused images. In overfocused images, the CNCs are clear with a dark outline which reminds the aspect they would have after negative staining. Close to zero defocus, the contrast is minimal and the specimen is hardly visible. Paradoxically, the operator will be satisfied by images recorded with some defocus as the contrast is higher and as the Fresnel fringes around the particles create an impression of "sharpness." However, this effect is associated with a loss of details. A satisfactory image is thus obtained by balancing the opposing requirements of contrast and ultrastructural details. By convention, the images are recorded in underfocused conditions, the amount of applied defocus increasing with decreasing magnification (typically about -5 μm at 3000x and -1 μm at 10000x). The importance of using underfocused conditions is clear in the case of negatively stained specimens, as seen in Figure 8b.

In the routine observation of unstained CNCs, three types of contrast contribute: a weak amplitude contrast due to the small size and organic nature of the particles; a significant diffraction contrast that depends on the crystallinity index of cellulose and orientation of the particles with respect to the incident electron beam; a phase contrast that generate Fresnel fringes along the CNCs controlled by the amount of defocus. As detailed in the following section, all these contributions will be affected by radiation damage.

2.3.2. Radiation damage

The most important limitation to observe crystalline polymers by TEM is the significant damage created by the electron beam which rapidly affects the resolution and decreases the

http://dx.doi.org/10.5772/60985

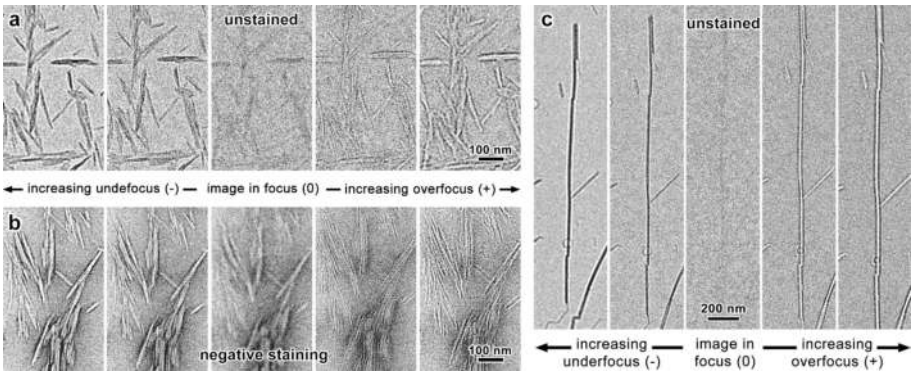

Figure 8. Influence of the defocus on the contrast of cotton (a,b) and tunicate (c) CNCs. The preparations are unstained (a,c) and negatively stained with uranyl acetate (b).

contrast of the objects. In such low-density materials, the inelastic scattering of the electrons generates molecular excitations and ionization phenomena, resulting in local heating of the material, breaking of covalent bonds, diffusion of free radicals, and emission of volatile species [86]. The consequences can be mass loss, fusion, vaporization, loss of crystallinity, all resulting in a significant decrease of amplitude, diffraction, and Fresnel contrasts. For crystalline materials, one can define a "lethal" or "total end point" dose by monitoring the disappearance of the electron diffraction pattern and calculating the electron dose at which crystallinity is irreversibly lost.

Even if the selected microscope has the ability to visualize details down to a resolution of 0.1-0.2 nm, the sample itself imposes drastic constraints. Several solutions exist to limit the detrimental effects of beam damage during the observation and image recording. First, contrary to what is done with materials made of heavy atoms, increasing the accelerating voltage of the electrons decreases the interactions with the polymer and thus increases the lethal dose (typically about a factor of 2 between 100 and 200 kV). However, the consequence of a higher accelerating voltage is a decrease in contrast. For instance, individual CNCs observed at 200 kV or a higher voltage tend to become transparent.

Second, the operator has to work with electron doses much lower than the lethal dose, which requires both to use low magnifications and significantly decrease the illumination (*e.g.*, by changing the "spot size" and spreading the surface of illumination). The observation of unstained cellulose specimens thus requires for the operator to make a compromise between image magnification (to see fine details with a sufficient contrast) and electron dose (to have a sufficient signal-to-noise ratio for the detector recording the image). Chanzy has quantified the lethal dose of cellulose by submitting *Valonia* CMFs to increasing electron doses at various accelerating voltages and monitoring the decay of diffracted beam intensity [87]. The average value for the lethal dose was about 4 electrons.$Å^{-2}$, which illustrates the extreme sensitivity of polysaccharides.

Third, the radiation damage can be significantly slowed down (but not suppressed) when the diffusion of free radicals is reduced by maintaining the specimen at low temperature, using a specific specimen holder cooled down with liquid nitrogen. In that case, an increase of the lethal dose by a factor of 3 has been reported in the literature.

The images in Figure 9 qualitatively illustrate the cumulative effect of beam damage during the observation of CNCs. Cotton and tunicate CNCs (Figures 9a and 9b, respectively) have been submitted to increasing electron doses. The three contributions to contrast previously mentioned are affected: diffraction contrast by disruption of the crystallinity; amplitude contrast by mass loss; and phase contrast by thinning of the particle and surface damage. The CNCs become transparent and their shape less well-defined. These effects are very fast and irreversible, in particular if the specimen is readily observed at magnifications above 10000x or the beam is inadvertently focused into a smaller disk (Figure 9c).

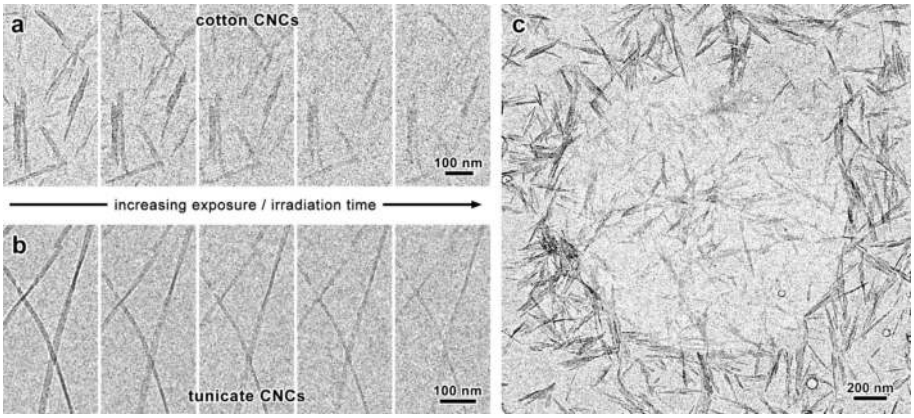

Figure 9. Influence of the radiation damage on the contrast of unstained cotton (a) and tunicate (b) CNCs. In (c), the electron beam has been briefly condensed into a smaller disk resulting in a marked damage on a distribution of unstained cotton CNCs.

2.3.3. 3D imaging

TEM images are two-dimensional (2D) projections of the 3D objects along the beam direction. Information along this direction is thus lost. One 2D image is generally not enough for the viewer to have a clear idea of the 3D shapes and several images, recorded at different tilt angles of the specimen, are necessary to make a reliable morphological analysis. Electron tomography (ET) can be performed in modern microscopes, thanks to the use of digital cameras and software that can precisely control the specimen orientation and image acquisition. Briefly, series of 2D images containing the data for mass-density distribution in the specimen are automatically recorded with small angular increments over a large angular range (usually from +70° to -70°). Using specific software, the collected images are aligned with respect to one another and a back-projection is carried out to obtain a 3D reconstruction of the specimen

volume [88-90]. While this technique is now widely used to study the morphology and structure of biological systems (proteins, viruses, membranes, etc.), So far, only two cases of CNC analysis can be found in the literature and will be described in § 3.4 [44, 62]. As explained in § 2.3.2, unstained cellulose is highly sensitive to beam damage and will be rapidly degraded. The amplitude contrast will thus decrease during the recording of the tilt series. This necessitates working at low magnification, with extremely low electron doses and a sensitive digital camera. In addition, due to the crystalline nature of CNCs, the contribution of diffraction contrast may fluctuate depending on the tilt angle of the particles.

3. Review of cellulose nanocrystal imaging and size analysis

3.1. TEM images and size distributions of CNCs

Although AFM is still often used to perform size measurements of CNC populations [15, 16, 57-59], TEM has been a method of choice to visualize the shape and structure of individual or bundled CNCs [16, 60, 91, 92]. The images are consistent and show that CNCs are rodlike and have a high aspect ratio. Some authors have observed spherical CNC particles [79] but these have been shown to be aggregation-induced artifacts [78]. As seen in Figure 2, the CNC aspect ratio and structure greatly vary with the cellulose source. CNCs obtained from plant sources like cotton [60, 93, 94], rice [95, 96], ramie [97-99], sisal [99, 100], or sugar beet [94] have smaller aspect ratios than those of bacterial cellulose [101, 102], microcrystalline cellulose (MCC) [51, 98, 103-106] and tunicin [98] (Table 1). The significant heterogeneity of the length and width distributions of CNCs, for a given source of cellulose, can be attributed to the method of preparation: type and concentration of the acid, reaction time, temperature, sonication, method of drying, etc.

Source of Cellulose		Length (nm)	Width (nm)	References*
Plants	Cotton	50–300	5–10	[60, 94]
	Rice	50–300	10–15	[95, 96]
	Ramie	50–250	5–10	[97-99]
	Sisal	100–200	3–7	[100, 107]
Microcrystalline cellulose (MCC) from wood		50–500	5–50	[103, 104, 106, 108]
Tunicates		100–3000	10–50	[60, 94, 109, 110]
Bacteria		200–3000	10–75	[101, 102, 105]

*Proposed references are representative examples and do not constitute an exhaustive list.

Table 1. Size distribution of CNCs from various sources of cellulose.

To a first approximation, the size measurement of CNCs should not be particularly difficult, provided that the objects are fairly well individualized on the supporting films, not severely

damaged by the electron beam (§ 2.3.2), and that a reasonable underfocus was used to record the image (§ 2.3.1). Their length and width can be measured from general views recorded at intermediate magnifications (typically 5000 to 10000×) by using a software like ImageJ [111]. Automated procedures are generally difficult to implement with TEM micrographs as the preliminary binarization of the images requires to clearly distinguish the CNCs from a continuous background. As seen in many images presented in this article, this is rarely the case. Thus, one directly uses the measurement tools of the software or outlines each CNC so that a semiautomatic measurement routine can be run. In addition, a review of the literature shows that the number of counted particles greatly varies (typically from 100 to 1000), mostly depending on the number of individual particles in the images and the patience of the operator. Of course, the number of objects taken into account will influence the reliability of the population statistics.

When higher magnifications are used (typically, 10000 to 50000×), keeping in mind the potential beam damage of unstained specimens, a better resolution is achieved and more details are revealed, particularly after negative staining. As confirmed by many images found in the literature, the majority of CNCs prepared from various sources are not single crystallites. They are often composed of a few laterally joined rodlike crystallites, as illustrated by Figure 10 in the case of cotton CNCs. The same feature has been reported for tunicate [60], Avicel [60], or bamboo [12] CNCs, to give just a few examples. The images in Figure 10 clearly show that cotton CNCs have a high variability in shape and dimensions. They are all different in size and structure, being composed of different numbers of unit crystallites, joined in a different fashion. This association inside individual particles does not result from artifactual flocculation but rather from the fact that the hydrolysis was performed on dry cellulosic substrates in which microfibrils are strongly linked by hydrogen bonds. Neither acid hydrolysis nor sonication (nor any high-shearing device) could fully separate the constituting crystallites.

The composite nature of most CNCs, which was validated by a combination of imaging and scattering techniques [12, 60], will thus influence the measurement of the lateral dimensions which depend on the cross-sectional shape and its regularity along the whole particle, the existence of a longitudinal twist, and the specimen preparation method. Considering the acicular morphology of CNCs, their distribution on a supporting film or inside thin vitreous ice favors their planar orientation, allowing to easily measure the length of the rodlike nanoparticles. However, while the particle thickness can be accurately measured from tapping mode AFM images, a choice has to be made regarding the definition of the width in TEM micrographs. As many types of CNCs exhibit a spindle-like shape, the width is generally defined as the largest dimension perpendicular to the particle long axis. Moreover, when the CNCs are ribbon-like, because of the rectangular cross section of individual crystallites (tunicate CNCs, for instance) or the lateral association of crystallites (cotton CNCs), the drying on a supporting film will generate a strong uniplanarity, the particles tending to lie on their widest face. This propensity to uniplanarity, which brings very useful information of the crystallite orientation in the CNCs, can be easily evaluated by performing complementary WAXS analysis on air-dried films [12, 60]. In addition, some CNCs are longitudinally twisted, which can be detected in TEM images by variations in contrast or stain distribution along the

http://dx.doi.org/10.5772/60985

particle (an example on tunicate CNCs can be seen in Figure 9b). Therefore, the apparent width of the particle will vary, making the choice of a relevant region to measure more difficult.

Cryo-TEM has been shown to be helpful in preventing particle aggregation/agglomeration due to drying [60, 82]. If the suspension concentration has been chosen with care, and considering the fact that CNCs have charges on their surface, they are conveniently individualized in the embedding film of vitreous ice. As their lateral dimensions are smaller than the typical thickness of the liquid film prior to fast-freezing, they could freely rotate around their long axis. Consequently, the measured width indeed corresponds to the projection of the CNC in a given orientation. Therefore, the width distribution of the population from a cryo-TEM image provides a rotational average of the lateral dimension of the particle and can thus be different from the distribution that is obtained from a specimen prepared by air-drying on a supporting film. The effect will be more pronounced for flat particles, such as cotton CNCs, as shown in Figure 10. Using a simple model, Elazzouzi-Hafraoui *et al.* have described the relation that can be made between the distributions obtained with both preparation techniques [60].

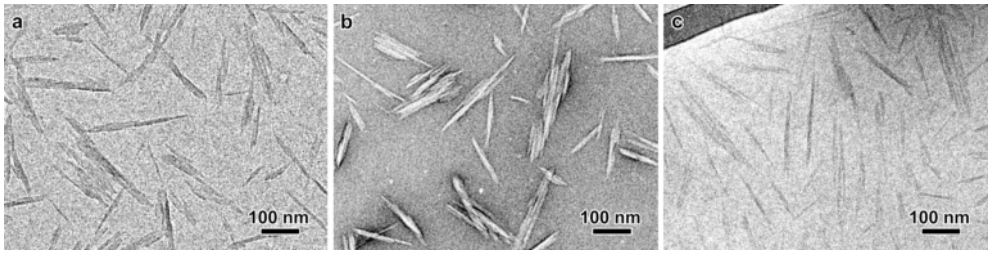

Figure 10. TEM images illustrating the diversity of shapes and structures of CNCs prepared by acid hydrolysis of cotton linters: a) dry specimen; b) negative staining (courtesy of F. Azzam, CERMAV); c) cryo-TEM (courtesy of S. Elazzouzi-Hafraoui, CERMAV).

Determining a size distribution from TEM images thus implies clearly stating the choices that were made in relation with the particle morphology. In addition, length and width distribution can be determined independently (Figure 11a) [78, 82] or assuming that there is a correlation between longitudinal and lateral dimensions of the CNCs. In that case, length and width are tabulated for each particle, resulting in a 2D size distribution histogram (Figure 11b) which validates (or not) the correlation [60].

The relevance of the size distribution of a given population of CNCs depends on several factors in relation with the problem that is addressed or the specific property that is investigated. For acicular (and possibly ribbon-like) CNCs, the influence of the statistical errors on the measurements will differ depending on the considered dimension (smaller for the length and larger for the width and thickness). Moreover, the size distributions are always wide, with large standard deviations and asymmetrical shapes (Figure 11) [16, 82, 91, 92]. Average lengths, widths, and thicknesses provide a cylindrical average view of the particles that can be useful to build a preliminary model. However, it is likely that a more complete description of the population, made by fitting the data with suitable functions, will be more relevant for

comparisons with X-ray or neutron scattering results [60], or, for example, to understand the percolation behavior of CNCs inside nanocomposite materials.

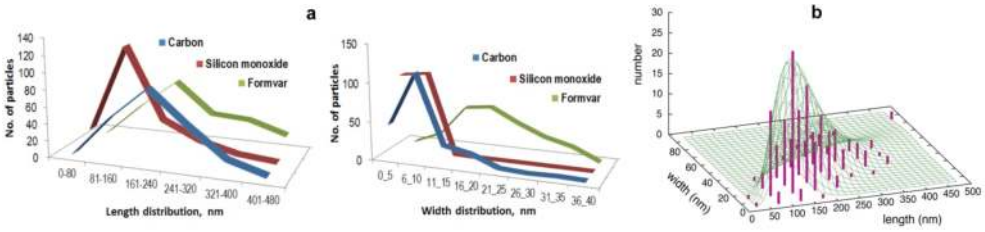

Figure 11. Length and width distributions histograms of various CNC systems determined from TEM images: a) never-dried CNCs at pH 3.5 deposited on different types of grids and observed unstained [78]; b) 2D histogram from negatively stained cotton CNCs (reprinted with permission from [60]. Copyright 2008 American Chemical Society).

3.2. TEM of CNC-hybrid composites

Hybrid composites of CNC with metal nanoparticles (NPs) such as Ag [39, 46, 112], Au [39, 41], Cu [39], Pd [40, 44, 113], Pt [39, 114], or Se [115] have been reported. TEM, along with its analytical tools, was used to characterize such composites (Figure 12). Due to their high atomic number and possible crystallinity, the metal NPs appear as dark spots in underfocused images. The difficulty to observe such hybrid organic-inorganic systems comes from the fact that CNCs and metal NPs have very different sensitivity to beam damage. While metallic NPs are very stable, cellulose is rapidly damaged, resulting in a significant loss of contrast and recognizable morphology. Consequently, to have a better visibility, a large defocus is usually applied which causes an overestimation in the size of metal NPs [78]. Additional negative staining can be effective to outline the CNCs more precisely but care must be taken to prevent the layer of stain from overshadowing the contrast of the metallic nanoclusters. Indeed, if the metallic NPs are smaller than 3-4 nm, they will not be distinguished from the granularity of the dry stain. As shown in Figure 12f, for larger NPs, CNCs can benefit from the negative staining while the metallic clusters still appears as dark spots. Finally, recent results demonstrated that highly sensitive direct detection device (DDD) cameras, associated with phase plates, allowed to observe simultaneously CNCs and subnanometer-thick palladium plates at their surface (Figure 13) [44]. In this experiment, the organic and inorganic phases were observed together at near-focus conditions.

Alongside visualization of metal NPs, it is very important to validate the chemical nature of the NPs seen in the images. This analysis can be done in a TEM by using energy-dispersive X-ray spectroscopy (EDX) which allows for quantitative measurement of the chemical composition [40].

http://dx.doi.org/10.5772/60985

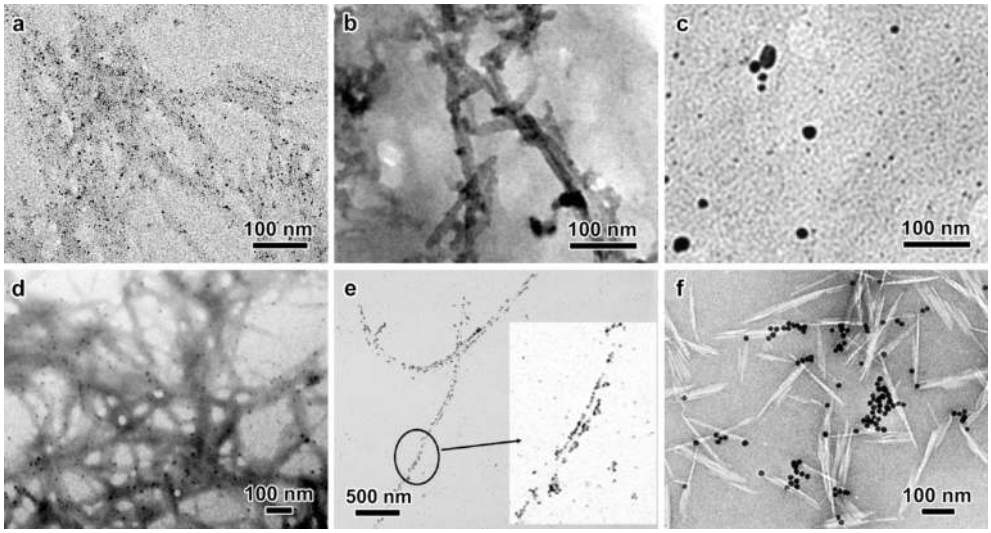

Figure 12. Hybrid systems with metallic nanoparticles supported by CNCs: a) Pd on wood pulp CNCs (reproduced from [40] by permission of The Royal Society of Chemistry); b) Pt on cotton CNCs (reproduced from [114] by permission of The Royal Society of Chemistry); c) Ag on cotton CNCs (reprinted with permission from [112]. Copyright 2014 American Chemical Society); d) Au on wood pulp CNCs (reproduced from [41] by permission of The Royal Society of Chemistry); e) Cu on tunicate CNCs (reprinted with permission from [39]. Copyright 2010 American Chemical Society); f) colloidal gold nanoparticles in interaction with cotton CNCs (negative staining) (courtesy of B. Jean, CERMAV – unpublished results).

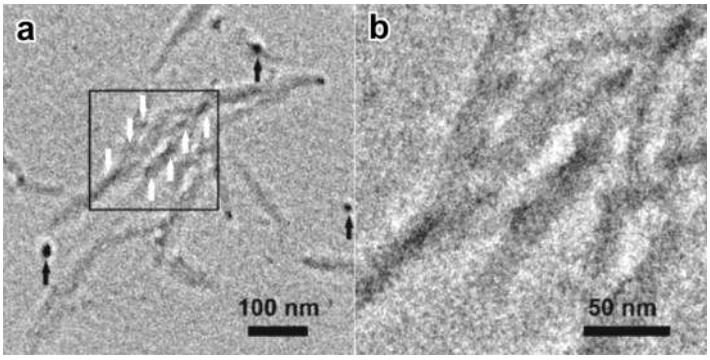

Figure 13. TEM images of patches of Pd onto CNCs recorded using a DDD camera: a) the white arrows point at Pd plates located on the surface of isolated CNCs. The black arrows point at larger and darker NPs that are not physically linked to CNCs; b) close-up view of the area indicated by the box on the left and revealing Pd patches (reprinted with permission from [44]. Copyright 2015 American Chemical Society).

3.3. TEM of CNC-polymer nanocomposites

Due to their nanoscale dimensions, high surface area, low density, and high mechanical strength, CNCs have been incorporated as reinforcing component into various polymer matrices: styrene-butyl acrylate [14, 27] polylactic acid [116, 117], poly(vinylalcohol) [118], polyurethane [119, 120], epoxy [121], and polyvinylacetate [100, 122]. In order to explain the variation in mechanical properties, these bulk materials have often been characterized by SEM after fracturing, allowing to visualize the distribution of CNCs that emerge at the fracture surface. However, SEM remained limited to the characterization of the topography of the fracture surfaces. TEM was also used to visualize the CNCs inside the material *via* preparation by ultramicrotomy of ultrathin sections of the composites. Figure 14 shows examples of images of nanocomposites of CNCs in matrices of styrene-butyl acrylate [14] and polyurethane [120]. CNCs can be visualized using their intrinsic diffraction contrast [14] but, as they are very sensitive to beam damage, their contrast rapidly decreases to the point where they become hardly visible with the polymer matrix due to the lack of density difference. Additional staining of the matrix can be used, for instance with OsO_4, creating a negative staining effect revealing the embedded CNCs [121].

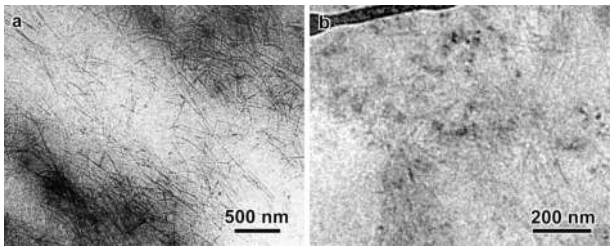

Figure 14. TEM images of ultrathin sections of nanocomposite materials incorporating CNCs as reinforcing component: a) tunicate CNCs in a matrix of styrene-butyl acrylate – diffraction contrast in bright field mode (reprinted with permission from [14]. Copyright 1995 American Chemical Society); b) thin cryosection of a cotton CNC/polyurethane composite observed under cryo-TEM conditions (reprinted with permission from [120]. Copyright 2011 American Chemical Society)

3.4. 3D imaging of CNCs and polymer-wrapped CNCs

Electron tomography (described in § 2.3.3) has only very recently begun to be used to characterize cellulose-based architectures or individual particles. Ciesielski *et al.* have recently published ET reconstructions of treated plant cell walls, allowing to get 3D information on the microfibril morphology [123]. Majoinen *et al.* studied the morphology of individual CNCs embedded in vitreous ice. Using cryo-TEM conditions, they recorded tilt series and reconstructed tomograms from pristine CNCs (Figure 15a) and from CNCs wrapped up with dendronized polymers (Figure 15b). This 3D visualization of the CNCs revealed the presence of an helicoidal twist along the rodlike particles. These twists have been proposed to be significant in explaining the cholesteric liquid crystalline assembly [18, 19] and their use in chiral templating [32, 33]. More recently, tomograms of ice-embed-

ded Pd modified CNCs were also useful to gain insight into the nature of the material under close-to-catalysis conditions [44].

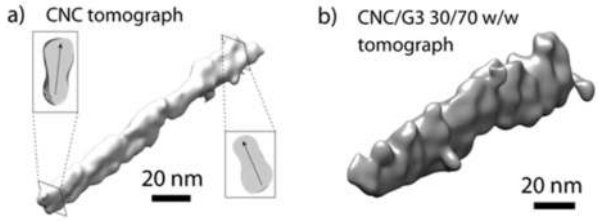

Figure 15. Electron tomography reconstitution of initial (a) and dendronized (b) polymer-wrapped cotton CNCs (reprinted with permission from [62]. Copyright 2014 American Chemical Society).

4. Conclusion and perspectives: Challenges and solutions in imaging CNCs

CNCs have been extensively studied and many reports can be found in the literature. The particle shape and size vary as a function of the cellulose source and the methodology used to produce the CNCs. In all cases, the CNC populations are polydisperse, featuring wide and asymmetrical size distributions. An accurate knowledge of the CNC dimensions and size distribution is crucial to characterize the properties of individual particles and their assemblies in suspension, in dry films or after incorporation into matrices. For instance, morphology and size will influence the phase separation behavior and the formation of liquid crystalline organizations or the percolation properties in nanocomposites. The development of chemical modifications strategies also requires a good knowledge of the accessible surface. In addition, CNCs have recently become a new type of industrial nanomaterial with numerous exciting properties, and an accurate characterization is important to optimize processes and control their reproducibility.

TEM is a key imaging technique to achieve this goal, thanks to the development of specific techniques to observe beam-sensitive polymers. Cellulose is without doubt one of the most beam-sensitive materials that can be observed by TEM. Consequently, special care must be taken to record reliable images of CNCs (low dose, low temperature, additional staining). In this article, we have described several sample preparation procedures and observation techniques adapted to the recording of images of CNC populations and have carried out reliable size distribution analyses. New approaches have recently been proposed, taking advantage of technical improvements of the microscopes, such as a better control of the stage movements, the use of highly sensitive digital cameras, and automatized corrections of several optical aberrations, allowing to record electron tomography image series and reconstruct the volume of the specimens. Although these sophisticated approaches are not routinely used yet

in the field of cellulose science, they will certainly rapidly develop. In addition, at a time when the research on CNCs is booming and the range of commercial applications is expanding, TEM imaging will continue to play a central role. Automated particle measurement procedures using TEM image analysis software will be needed to streamline quality control.

Acknowledgements

The TEM images in Figures 3, 8, and 9 were specifically recorded for this chapter by J.-L. Putaux on a Philips CM200 microscope operating at an accelerating voltage of 200 kV and equipped with a TVIPS TemCam F216 camera. We thank the Electron Microscopy Platform of Institut de Chimie Moléculaire de Grenoble for granting access to this equipment.

Author details

Madhu Kaushik[1], Carole Fraschini[2], Grégory Chauve[2], Jean-Luc Putaux[3,4*] and Audrey Moores[1*]

*Address all correspondence to: audrey.moores@mcgill.ca, putaux@cermav.cnrs.fr

1 Centre for Green Chemistry and Catalysis, Department of Chemistry, McGill University, Montréal, QC, Canada

2 FPInnovations, Pointe-Claire (Québec), Canada

3 Université Grenoble Alpes, Centre de Recherches sur les Macromolécules Végétales (CERMAV), Grenoble, France

4 CNRS, CERMAV, Grenoble, France

Disclaimer: Mention of trademarks or commercial products in this article is solely for the purpose of providing examples of sample preparation materials and methods and does not imply any affiliation from the authors with the mentioned companies.

References

[1] Chinga-Carrasco G. Cellulose fibres, nanofibrils and microfibrils: the morphological sequence of MFC components from a plant physiology and fibre technology point of view. *Nanoscale Res Lett*. 2011; 6 (1): 1-7.

[2] Nishiyama Y. Structure and properties of the cellulose microfibril. *J Wood Sci*. 2009; 55 (4): 241-9.

[3] Klemm D, Philipp B, Heinze T, Heinze U, Wagenknecht W. *Comprehensive Cellulose Chemistry 1. Fundamentals And Analytical Methods*. Weinheim: Wiley-VCH; 1998.

[4] Klemm D, Heublein B, Fink HP, Bohn A. Cellulose: fascinating biopolymer and sustainable raw material. *Angew Chem Int Ed*. 2005; 44 (22): 3358-93.

[5] Nickerson RF, Habrle JA. Cellulose intercrystalline structure. *Ind Eng Chem*. 1947; 39 (11): 1507-12.

[6] Rånby BG. Aqueous colloidal solutions of cellulose micelles. *Acta Chem Scand*. 1949; 3 (1): 649-50.

[7] Rånby BG. Fibrous macromolecular systems. Cellulose and muscle. The colloidal properties of cellulose micelles. *Discuss Faraday Soc*. 1951; 11: 158-64.

[8] Revol J-F, Bradford H, Giasson J, Marchessault RH, Gray DG. Helicoidal self-ordering of cellulose microfibrils in aqueous suspension. *Int J Biol Macromol*. 1992; 14 (3): 170-2.

[9] Mukherjee SM, Woods HJ. X-ray and electron microscope studies of the degradation of cellulose by sulphuric acid. *Biochim Biophys Acta*. 1953; 10: 499-511.

[10] Rånby B. Physico-chemical investigations on bacterial cellulose. *Arkiv for Kemi*. 1952; 4 (3): 249.

[11] Fraschini C, Chauve G, Berre J-FL, Ellis S, Méthot M, O'Connor B, et al. Critical discussion of light scattering and microscopy techniques for CNC particle sizing. *Nord Pulp Pap Res J*. 2014; 29 (1): 31-40.

[12] Brito BS, Pereira FV, Putaux J-L, Jean B. Preparation, morphology and structure of cellulose nanocrystals from bamboo fibers. *Cellulose*. 2012; 19 (5): 1527-36.

[13] Lopez M, Bizot H, Chambat G, Marais M-F, Zykwinska A, Ralet M-C, et al. Enthalpic studies of xyloglucan–cellulose interactions. *Biomacromolecules*. 2010; 11 (6): 1417-28.

[14] Favier V, Chanzy H, Cavaillé J-Y. Polymer nanocomposites reinforced by cellulose whiskers. *Macromolecules*. 1995; 28 (18): 6365-7.

[15] Le Normand M, Moriana R, Ek M. Isolation and characterization of cellulose nanocrystals from spruce bark in a biorefinery perspective. *Carbohydr Polym*. 2014; 111: 979-87.

[16] Silvério HA, Neto WPF, Dantas NO, Pasquini D. Extraction and characterization of cellulose nanocrystals from corncob for application as reinforcing agent in nanocomposites. *Ind Crops Prod*. 2013; 44: 427-36.

[17] Eichhorn SJ, Dufresne A, Aranguren M, Marcovich NE, Capadona JR, Rowan SJ, et al. Review: current international research into cellulose nanofibres and nanocomposites. *J Mater Sci*. 2010; 45 (1): 1-33.

[18] Habibi Y, Lucia LA, Rojas OJ. Cellulose nanocrystals: chemistry, self-assembly, and applications. *Chem Rev*. 2010; 110 (6): 3479-500.

[19] Klemm D, Kramer F, Moritz S, Lindström T, Ankerfors M, Gray D, et al. Nanocelluloses: a new family of nature-based materials. *Angew Chem Int Ed*. 2011; 50 (24): 5438-66.

[20] Moon RJ, Martini A, Nairn J, Simonsen J, Youngblood J. Cellulose nanomaterials review: structure, properties and nanocomposites. *Chem Soc Rev*. 2011; 40 (7): 3941-94.

[21] Lin N, Huang J, Dufresne A. Preparation, properties and applications of polysaccharide nanocrystals in advanced functional nanomaterials: a review. *Nanoscale*. 2012; 4 (11): 3274-94.

[22] Salas C, Nypelö T, Rodriguez-Abreu C, Carrillo C, Rojas OJ. Nanocellulose properties and applications in colloids and interfaces. *Curr Opin Colloid Interface Sci*. 2014; 19 (5): 383-96.

[23] Azzam F, Heux L, Putaux J-L, Jean B. Preparation by grafting onto, characterization, and properties of thermally responsive polymer-decorated cellulose nanocrystals. *Biomacromolecules*. 2010; 11 (12): 3652-9.

[24] Lam E, Male KB, Chong JH, Leung ACW, Luong JHT. Applications of functionalized and nanoparticle-modified nanocrystalline cellulose. *Trends Biotechnol*. 2012; 30 (5): 283-90.

[25] Beck S, Bouchard J, Berry R. Dispersibility in water of dried nanocrystalline cellulose. *Biomacromolecules*. 2012; 13 (5): 1486-94.

[26] Marchessault RH, Morehead FF, Walter NM. Liquid crystal systems from fibrillar polysaccharides. *Nature*. 1959; 184 (4686): 632-3.

[27] Favier V, Canova G, Cavaillé J-Y, Chanzy H, Dufresne A, Gauthier C. Nanocomposite materials from latex and cellulose whiskers. *Polym Adv Technol*. 1995; 6 (5): 351-5.

[28] Revol J-F, Godbout L, Dong X-M, Gray DG, Chanzy H, Maret G. Chiral nematic suspensions of cellulose crystallites; phase separation and magnetic field orientation. *Liq Cryst*. 1994; 16 (1): 127-34.

[29] Picard G, Simon D, Kadiri Y, LeBreux J, Ghozayel F. Cellulose nanocrystal iridescence: a new model. *Langmuir*. 2012; 28 (41): 14799-807.

[30] Liu D, Wang S, Ma Z, Tian D, Gu M, Lin F. Structure–color mechanism of iridescent cellulose nanocrystal films. *RSC Adv*. 2014; 4 (74): 39322-31.

[31] Chen Q, Liu P, Nan F, Zhou L, Zhang J. Tuning the iridescence of chiral nematic cellulose nanocrystal films with a vacuum-assisted self-assembly technique. *Biomacromolecules*. 2014; 15 (11): 4343-50.

[32] Shopsowitz KE, Qi H, Hamad WY, MacLachlan MJ. Free-standing mesoporous silica films with tunable chiral nematic structures. *Nature*. 2010; 468 (7322): 422-5.

[33] Shopsowitz KE, Kelly JA, Hamad WY, MacLachlan MJ. Biopolymer templated glass with a twist: controlling the chirality, porosity, and photonic properties of silica with cellulose nanocrystals. *Adv Funct Mater*. 2014; 24 (3): 327-38.

[34] Shopsowitz KE, Hamad WY, MacLachlan MJ. Chiral nematic mesoporous carbon derived from nanocrystalline cellulose. *Angew Chem Int Ed*. 2011; 50 (46): 10991-5.

[35] Querejeta-Fernández A, Chauve G, Methot M, Bouchard J, Kumacheva E. Chiral plasmonic films formed by gold nanorods and cellulose nanocrystals. *J Am Chem Soc*. 2014; 136 (12): 4788-93.

[36] Serizawa T, Sawada T, Wada M. Chirality-specific hydrolysis of amino acid substrates by cellulose nanofibers. *Chem Commun*. 2013; 49 (78): 8827-9.

[37] Yang J, Han C-R, Duan J-F, Ma M-G, Zhang X-M, Xu F, et al. Studies on the properties and formation mechanism of flexible nanocomposite hydrogels from cellulose nanocrystals and poly (acrylic acid). *J Mater Chem*. 2012; 22 (42): 22467-80.

[38] Yang X, Cranston ED. Chemically cross-linked cellulose nanocrystal aerogels with shape recovery and superabsorbent properties. *Chem Mater*. 2014; 26 (20): 6016-25.

[39] Padalkar S, Capadona JR, Rowan SJ, Weder C, Won Y-H, Stanciu LA, et al. Natural biopolymers: novel templates for the synthesis of nanostructures. *Langmuir*. 2010; 26 (11): 8497-502.

[40] Cirtiu CM, Dunlop-Brière AF, Moores A. Cellulose nanocrystallites as an efficient support for nanoparticles of palladium: application for catalytic hydrogenation and Heck coupling under mild conditions. *Green Chem*. 2011; 13 (2): 288.

[41] Lam E, Hrapovic S, Majid E, Chong JH, Luong JHT. Catalysis using gold nanoparticles decorated on nanocrystalline cellulose. *Nanoscale*. 2012; 4 (3): 997-1002.

[42] Zhou P, Wang H, Yang J, Tang J, Sun D, Tang W. Bacteria cellulose nanofibers supported palladium(0) nanocomposite and its catalysis evaluation in Heck reaction. *Ind Eng Chem Res*. 2012; 51 (16): 5743-8.

[43] Rezayat M, Blundell RK, Camp JE, Walsh DA, Thielemans W. Green one-step synthesis of catalytically active palladium nanoparticles supported on cellulose nanocrystals. *ACS Sustain Chem Eng*. 2014; 2 (5): 1241-50.

[44] Kaushik M, Basu K, Benoit C, Cirtiu CM, Vali H, Moores A. Cellulose nanocrystals as chiral inducers: enantioselective catalysis and transmission electron microscopy 3D characterization. *J Am Chem Soc*. 2015; 137 (19): 6124-7.

[45] Wu X, Lu C, Zhou Z, Yuan G, Xiong R, Zhang X. Green synthesis and formation mechanism of cellulose nanocrystal-supported gold nanoparticles with enhanced catalytic performance. *Environ Sci Nano*. 2014; 1 (1): 71-9.

[46] Xiong R, Lu C, Zhang W, Zhou Z, Zhang X. Facile synthesis of tunable silver nanostructures for antibacterial application using cellulose nanocrystals. *Carbohydr Polym*. 2013; 95 (1): 214-9.

[47] Kovacs T, Naish V, O'Connor B, Blaise C, Gagné F, Hall L, et al. An ecotoxicological characterization of nanocrystalline cellulose (NCC). *Nanotoxicology*. 2010; 4 (3): 255-70.

[48] Celluforce [cited 2015 29 March 2015]. Available from: http://celluforce.com/en/.

[49] Charreau H, L Foresti M, Vazquez A. Nanocellulose patents trends: a comprehensive review on patents on cellulose nanocrystals, microfibrillated and bacterial cellulose. *Recent Pat Nanotech*. 2013; 7 (1): 56-80.

[50] Husemann E CA. Über die Lagerung der Lockerstellen yon Cellulosemolekülen in der Faser. *Naturwissenschaften*. 1944; 32: 79-80.

[51] Dong XM, Kimura T, Revol J-F, Gray DG. Effects of ionic strength on the isotropic −chiral nematic phase transition of suspensions of cellulose crystallites. *Langmuir*. 1996; 12 (8): 2076-82.

[52] Elazzouzi-Hafraoui S, Putaux J-L, Heux L. Self-assembling and chiral nematic properties of organophilic cellulose nanocrystals. *J Phys Chem B*. 2009; 113 (32): 11069-75.

[53] Shafiei-Sabet S, Hamad WY, Hatzikiriakos SG. Rheology of nanocrystalline cellulose aqueous suspensions. *Langmuir*. 2012; 28 (49): 17124-33.

[54] Shafiei-Sabet S, Hamad W, Hatzikiriakos S. Ionic strength effects on the microstructure and shear rheology of cellulose nanocrystal suspensions. *Cellulose*. 2014; 21 (5): 3347-59.

[55] Derakhshandeh B, Petekidis G, Sabet SS, Hamad WY, Hatzikiriakos SG. Ageing, yielding, and rheology of nanocrystalline cellulose suspensions. *J Rheol*. 2013; 57 (1): 131-48.

[56] Helbert W, Nishiyama Y, Okano T, Sugiyama J. Molecular Imaging of Halocynthia papillosa Cellulose. *J Struct Biol*. 1998; 124 (1): 42-50.

[57] dos Santos RM, Neto WPF, Silvério HA, Martins DF, Dantas NO, Pasquini D. Cellulose nanocrystals from pineapple leaf, a new approach for the reuse of this agro-waste. *Ind Crops Prod*. 2013; 50: 707-14.

[58] Sacui IA, Nieuwendaal RC, Burnett DJ, Stranick SJ, Jorfi M, Weder C, et al. Comparison of the properties of cellulose nanocrystals and cellulose nanofibrils isolated from bacteria, tunicate, and wood processed using acid, enzymatic, mechanical, and oxidative methods. *ACS Appl Mater Inter*. 2014; 6 (9): 6127-38.

[59] Urena-Benavides EE, Brown PJ, Kitchens CL. Effect of jet stretch and particle load on cellulose nanocrystal− alginate nanocomposite fibers. *Langmuir*. 2010; 26 (17): 14263-70.

[60] Elazzouzi-Hafraoui S, Nishiyama Y, Putaux J-L, Heux L, Dubreuil F, Rochas C. The shape and size distribution of crystalline nanoparticles prepared by acid hydrolysis of native cellulose. *Biomacromolecules*. 2008; 9 (1): 57-65.

[61] Kalashnikova I, Bizot H, Bertoncini P, Cathala B, Capron I. Cellulosic nanorods of various aspect ratios for oil in water pickering emulsions. *Soft Matter*. 2013; 9 (3): 952-9.

[62] Majoinen J, Haataja JS, Appelhans D, Lederer A, Olszewska A, Seitsonen J, et al. Supracolloidal multivalent interactions and wrapping of dendronized glycopolymers on native cellulose nanocrystals. *J Am Chem Soc*. 2014; 136 (3): 866-9.

[63] Ruska H. Structure of cellulose fibers. *Kolloid-Z*. 1940; 92: 276-85.

[64] Eisenhut O, Kuhn E. Lichtmikroskopische und übermikroskopische Untersuchungen an natürlichen und künstlichen Cellulosefasern. *Angew Chem*. 1942; 55 (25-26): 198-206.

[65] Hambraeus G, Rånby B. Electron microscopic investigation of precipitates of cellulose nitrates. *Nature*. 1945; 155 (3929): 200-1.

[66] Husemann E CA. Elektronenmikroskopische Untersuchungen über submikroskopische Fibrillen aus Kunstfasern. *Makromol Chem*. 1947; 1: 158-63.

[67] Kinsinger WG, Hock CW. Electron microscopical studies of natural cellulose fibers. *Ind Eng Chem*. 1948; 40: 1711-6.

[68] Hock CW. Degradation of cellulose as revealed microscopically. *Text Res J*. 1950; 20 (3): 141-51.

[69] Rånby B, Ribi E. Über den feinbau der zellulose. *Experientia*. 1950; 6 (1): 12-4.

[70] Rånby B. Physico-chemical investigations on animal cellulose (Tunicin). *Arkiv for Kemi*. 1952; 4 (3): 241.

[71] Preston R, Ripley G. Electron diffraction diagrams of cellulose micro-fibrils in Valonia. *Nature*. 1954; 174: 76-7.

[72] Honjo G, Watanabe M. Examination of cellulose fibre by the low-temperature specimen method of electron diffraction and electron microscopy. *Nature*. 1958; 181: 326-8.

[73] Bourret A, Chanzy H, Lazaro R. Crystallite features of Valonia cellulose by electron diffraction and dark-field electron microscopy. *Biopolymers*. 1972; 11 (4): 893-8.

[74] Sugiyama J, Vuong R, Chanzy H. Electron diffraction study on the two crystalline phases occurring in native cellulose from an algal cell wall. *Macromolecules*. 1991; 24 (14): 4168-75.

[75] Koyama M, Helbert W, Imai T, Sugiyama J, Henrissat B. Parallel-up structure evidences the molecular directionality during biosynthesis of bacterial cellulose. *Proc Natl Acad Sci*. 1997; 94 (17): 9091-5.

[76] Sugiyama J, Harada H, Fujiyoshi Y, Uyeda N. Observations of cellulose microfibrils in Valonia macrophysa by high resolution electron microscopy. *J Jpn Wood Res Soc*. 1985; 31: 61-7.

[77] Sugiyama J, Harada H, Fujiyoshi Y, Uyeda N. Lattice images from ultrathin sections of cellulose microfibrils in the cell wall of Valonia macrophysa Kütz. *Planta*. 1985; 166 (2): 161-8.

[78] Kaushik M, Chen WC, van de Ven TGM, Moores A. An improved methodology for imaging cellulose nanocrystals by transmission electron microscopy. *Nord Pulp Pap Res J*. 2014; 29 (1): 77-84.

[79] Peng Y, Han Y, Gardner DJ. Spray-drying cellulose nanofibrils: effect of drying process parameters on particle morphology and size distribution. *Wood Fiber Sci*. 2012; 44 (4): 448-61.

[80] Peng Y, Gardner DJ, Han Y, Kiziltas A, Cai Z, Tshabalala MA. Influence of drying method on the material properties of nanocellulose I: thermostability and crystallinity. *Cellulose*. 2013; 20 (5): 2379-92.

[81] Harris JR. *Negative Staining and Cryoelectron Microscopy: The Thin Film Techniques. RMS Microscopy Handbook*. Oxford: BIOS Scientific Publishers; 1997.

[82] Abitbol T, Kloser E, Gray D. Estimation of the surface sulfur content of cellulose nanocrystals prepared by sulfuric acid hydrolysis. *Cellulose*. 2013; 20 (2): 785-94.

[83] Glauert AM. *Fixation, Dehydration and Embedding of Biological Specimens*. North-Holland/American: Elsevier; 1975.

[84] Reid N. *Practical Methods in Electron Microscopy: Ultramicrotomy*. North-Holland/American: Elsevier; 1975.

[85] Watt IM. *The Principles and Practice of Electron Microscopy*. Cambridge University Press; 1997.

[86] Grubb D. Radiation damage and electron microscopy of organic polymers. *J Mater Sci*. 1974; 9 (10): 1715-36.

[87] Chanzy H. Irradiation de la cellulose de Valonia au microscope à 1 MV. *BIST Commissariat à l'énergie Atomique*. 1975: 55-7.

[88] Fridman K, Mader A, Zwerger M, Elia N, Medalia O. Advances in tomography: probing the molecular architecture of cells. *Nat Rev Mol Cell Biol*. 2012; 13 (11): 736-42.

[89] Kremer JR, Mastronarde DN, McIntosh JR. Computer visualization of three-dimensional image data using IMOD. *J Struct Biol*. 1996; 116 (1): 71-6.

[90] Frank J. *Electron Tomography: Methods for Three-Dimensional Visualization of Structures in the Cell*. Springer Science & Business Media; 2008.

[91] Dong XM, Revol J-F, Gray DG. Effect of microcrystallite preparation conditions on the formation of colloid crystals of cellulose. *Cellulose*. 1998; 5 (1): 19-32.

[92] Henrique MA, Silvério HA, Neto WPF, Pasquini D. Valorization of an agro-industrial waste, mango seed, by the extraction and characterization of its cellulose nanocrystals. *J Environ Manage*. 2013; 121: 202-9.

[93] Rosa M, Medeiros E, Malmonge J, Gregorski K, Wood D, Mattoso L, et al. Cellulose nanowhiskers from coconut husk fibers: effect of preparation conditions on their thermal and morphological behavior. *Carbohydr Polym*. 2010; 81 (1): 83-92.

[94] Heux L, Chauve G, Bonini C. Nonflocculating and chiral-nematic self-ordering of cellulose microcrystals suspensions in nonpolar solvents. *Compos Interfaces*. 2000; 16 (21): 8210-2.

[95] Lu P, Hsieh Y-L. Preparation and characterization of cellulose nanocrystals from rice straw. *Carbohydr Polym*. 2012; 87 (1): 564-73.

[96] Johar N, Ahmad I, Dufresne A. Extraction, preparation and characterization of cellulose fibres and nanocrystals from rice husk. *Ind Crops Prod*. 2012; 37 (1): 93-9.

[97] Peresin MS, Habibi Y, Zoppe JO, Pawlak JJ, Rojas OJ. Nanofiber composites of polyvinyl alcohol and cellulose nanocrystals: manufacture and characterization. *Biomacromolecules*. 2010; 11 (3): 674-81.

[98] Habibi Y, Goffin A-L, Schiltz N, Duquesne E, Dubois P, Dufresne A. Bionanocomposites based on poly (ε-caprolactone)-grafted cellulose nanocrystals by ring-opening polymerization. *J Mater Chem*. 2008; 18 (41): 5002-10.

[99] Junior de Menezes A, Siqueira G, Curvelo AAS, Dufresne A. Extrusion and characterization of functionalized cellulose whiskers reinforced polyethylene nanocomposites. *Polymer*. 2009; 50 (19): 4552-63.

[100] Garcia de Rodriguez NL, Thielemans W, Dufresne A. Sisal cellulose whiskers reinforced polyvinyl acetate nanocomposites. *Cellulose*. 2006; 13 (3): 261-70.

[101] Roman M, Winter WT. Effect of sulfate groups from sulfuric acid hydrolysis on the thermal degradation behavior of bacterial cellulose. *Biomacromolecules*. 2004; 5 (5): 1671-7.

[102] Grunert M, Winter WT. Nanocomposites of cellulose acetate butyrate reinforced with cellulose nanocrystals. *J Polym Environ*. 2002; 10 (1-2): 27-30.

[103] Bondeson D, Mathew A, Oksman K. Optimization of the isolation of nanocrystals from microcrystalline cellulose by acid hydrolysis. *Cellulose*. 2006; 13 (2): 171-80.

[104] Capadona JR, Shanmuganathan K, Trittschuh S, Seidel S, Rowan SJ, Weder C. Polymer nanocomposites with nanowhiskers isolated from microcrystalline cellulose. *Biomacromolecules*. 2009; 10 (4): 712-6.

[105] Araki J, Kuga S. Effect of trace electrolyte on liquid crystal type of cellulose microcrystals. *Langmuir*. 2001; 17 (15): 4493-6.

[106] Araki J, Wada M, Kuga S, Okano T. Influence of surface charge on viscosity behavior of cellulose microcrystal suspension. *J Wood Sci*. 1999; 45 (3): 258-61.

[107] Siqueira G, Bras J, Dufresne A. Cellulose whiskers versus microfibrils: influence of the nature of the nanoparticle and its surface functionalization on the thermal and mechanical properties of nanocomposites. *Biomacromolecules*. 2008; 10 (2): 425-32.

[108] Araki J, Wada M, Kuga S, Okano T. Flow properties of microcrystalline cellulose suspension prepared by acid treatment of native cellulose. *Colloids Surf A*. 1998; 142 (1): 75-82.

[109] Anglès MN, Dufresne A. Plasticized starch/tunicin whiskers nanocomposites. 1. Structural analysis. *Macromolecules*. 2000; 33 (22): 8344-53.

[110] Kimura F, Kimura T, Tamura M, Hirai A, Ikuno M, Horii F. Magnetic alignment of the chiral nematic phase of a cellulose microfibril suspension. *Langmuir*. 2005; 21 (5): 2034-7.

[111] ImageJ. Available from: http://imagej.nih.gov/ij/.

[112] Lokanathan AR, Uddin KMA, Rojas OJ, Laine J. Cellulose nanocrystal-mediated synthesis of silver nanoparticles: role of sulfate groups in nucleation phenomena. *Biomacromolecules*. 2014; 15 (1): 373-9.

[113] Wu X, Lu C, Zhang W, Yuan G, Xiong R, Zhang X. A novel reagentless approach for synthesizing cellulose nanocrystal-supported palladium nanoparticles with enhanced catalytic performance. *J Mater Chem A*. 2013; 1 (30): 8645-52.

[114] Benaissi K, Johnson L, Walsh DA, Thielemans W. Synthesis of platinum nanoparticles using cellulosic reducing agents. *Green Chem*. 2010; 12 (2): 220-2.

[115] Shin Y, Blackwood JM, Bae I-T, Arey BW, Exarhos GJ. Synthesis and stabilization of selenium nanoparticles on cellulose nanocrystal. *Mater Lett*. 2007; 61 (21): 4297-300.

[116] Bondeson D, Oksman K. Dispersion and characteristics of surfactant modified cellulose whiskers nanocomposites. *Compos Interfaces*. 2007; 14 (7-9): 617-30.

[117] Petersson L, Kvien I, Oksman K. Structure and thermal properties of poly(lactic acid)/cellulose whiskers nanocomposite materials. *Compos Sci Technol*. 2007; 67 (11–12): 2535-44.

[118] Paralikar SA, Simonsen J, Lombardi J. Poly(vinyl alcohol)/cellulose nanocrystal barrier membranes. *J Membr Sci*. 2008; 320 (1-2): 248-58.

[119] Marcovich NE, Auad ML, Bellesi NE, Nutt SR, Aranguren MI. Cellulose micro/nanocrystals reinforced polyurethane. *J Mater Res*. 2006; 21 (04): 870-81.

[120] Pei A, Malho J-M, Ruokolainen J, Zhou Q, Berglund LA. Strong nanocomposite reinforcement effects in polyurethane elastomer with low volume fraction of cellulose nanocrystals. *Macromolecules*. 2011; 44 (11): 4422-7.

[121] Matos Ruiz M, Cavaillé J-Y, Dufresne A, Gérard J-F, Graillat C. Processing and characterization of new thermoset nanocomposites based on cellulose whiskers. *Compos Interfaces*. 2000; 7 (2): 117-31.

[122] Roohani M, Habibi Y, Belgacem NM, Ebrahim G, Karimi AN, Dufresne A. Cellulose whiskers reinforced polyvinyl alcohol copolymers nanocomposites. *Eur Polym J*. 2008; 44 (8): 2489-98.

[123] Ciesielski PN, Matthews JF, Tucker MP, Beckham GT, Crowley MF, Himmel ME, et al. 3D electron tomography of pretreated biomass informs atomic modeling of cellulose microfibrils. *ACS Nano.* 2013; 7 (9): 8011-9.